A Vertically Resolved Analysis of Radiative Feedbacks on Moist Static Energy Variance in Tropical Cyclones

BOSONG ZHANG,[a,b] BRIAN J. SODEN,[a] AND GABRIEL A. VECCHI[c,d]

[a] *Rosenstiel School of Marine and Atmospheric Science, University of Miami, Miami, Florida*
[b] *Program in Atmospheric and Oceanic Sciences, Princeton University, Princeton, New Jersey*
[c] *Department of Geosciences, Princeton University, Princeton, New Jersey*
[d] *High Meadows Environmental Institute, Princeton University, Princeton, New Jersey*

(Manuscript received 30 March 2022, in final form 24 October 2022)

ABSTRACT: A vertically resolved moist static energy (MSE) variance budget framework is used to diagnose processes associated with the development of tropical cyclones (TCs) in a general circulation model (GCM) under realistic boundary conditions. Previous studies have shown that interactions between radiation and MSE promote TC development. Here, we examine the vertical contributions of radiation and its interactions with MSE by performing several mechanism-denial experiments in which synoptic-scale radiative interactions are suppressed either in the boundary layer or in the free troposphere. Partly suppressing radiative interactions results in a reduction in global TC frequency. However, the magnitude of reduction and structure of the feedback depend on the intensity and structure of the TCs in these mechanism-denial experiments, indicating that both the magnitude and the vertical location of radiative interactions can impact global TC frequency. Using instantaneous 6-hourly outputs, an explicit computation reveals distinct spatial patterns of the advection term: the vertical component is positive in the mid- to upper troposphere, which reflects an upward transport of MSE by deep convection, whereas the horizontal component is positive in the boundary layer. These results illustrate the impact of the vertical distribution of radiative interactions and vertically varied contribution of the advection term in the development of TCs.

KEYWORDS: Advection; Radiation; Tropical cyclones; General circulation models

1. Introduction

In numerical simulations of radiative–convective equilibrium (RCE) without rotation, randomly distributed convection self-aggregates into organized clusters in the presence of idealized boundary conditions. Organized convective systems involve interactions between radiation, moisture, cloud, and circulation. An analysis framework based on a variance budget equation for the column-integrated moist static energy (MSE; Neelin and Held 1987) was introduced to understand aggregation-related physical processes (Wing and Emanuel 2014). With interactive radiation, the spatial contrast in radiative cooling induces a secondary low-level circulation that transports energy from dry to moist regions, which plays an important role in the aggregation process (Bretherton et al. 2005; Muller and Held 2012; Wing and Emanuel 2014; Muller and Bony 2015). Such enhanced low-level inflow was previously reported by Gray and Jacobson (1977) based on observations. In simulations with rotation, organized deep convective systems can appear in the form of tropical cyclones (TCs). Based on the variance budget equation for the column-integrated MSE, Wing et al. (2016) showed that the spontaneous development of a tropical cyclone from an initially homogeneous environment is promoted by feedbacks involving radiation and the surface fluxes. Similar results are also found in Muller and Romps (2018) in which cyclogenesis is accelerated in the presence of interactive radiation. In addition, recent studies used convection-permitting models to simulate observed TCs and showed the impact of radiation on different aspects of TCs (Melhauser and Zhang 2014; Tang and Zhang 2016; Tang et al. 2017, 2019). Overall, cloud radiative interactions promote the development of TCs (Melhauser and Zhang 2014; Nicholls 2015; Trabing et al. 2019; Rios-Berrios 2020; Ruppert et al. 2020; Smith et al. 2020; Wu et al. 2021). However, Wing et al. (2016) showed that the advection term, computed as a residual from the variance budget equation, contributes negatively to the development of TCs. Recently, Wing (2022) confirmed that the advection term is a negative contributor to the development of TCs when it is explicitly computed. Thus, the increase in spatial variance of TC-related MSE is primarily driven by diabatic heating.

In addition to numerical simulations under idealized settings, it is necessary to examine physical processes associated with TCs under realistic boundary conditions. General circulation models (GCMs) are useful tools that can provide long-term, global simulations of the climate system. Early studies showed that even low-resolution GCMs can simulate vortices that are similar to TCs (Manabe et al. 1970; Broccoli and Manabe 1990). However, biases are found in different aspects. On one hand, low-resolution GCMs tend to simulate fewer TCs than observations (Camargo 2013). On the other hand, TCs simulated in low-resolution GCMs are found to exhibit weaker intensity but larger size (Walsh et al. 2007; Vecchi et al. 2014; Murakami et al. 2015; Walsh et al. 2015; Camargo et al. 2020). While horizontal grid spacings do make a difference, the

Zhang's current affiliation: Program in Atmospheric and Oceanic Sciences, Princeton University, Princeton, New Jersey.

Corresponding author: Bosong Zhang, bosongzhang@gmail.com

DOI: 10.1175/JCLI-D-22-0199.1

© 2023 American Meteorological Society. For information regarding reuse of this content and general copyright information, consult the AMS Copyright Policy (www.ametsoc.org/PUBSReuseLicenses).

Brought to you by NOAA Central Library | Unauthenticated | Downloaded 01/30/24 02:51 PM UTC

TABLE 1. The 17 vertical pressure levels for the outputs in HiRAM and their layer thickness.

Pressure levels (hPa)	1000	925	850	700	600	500	400	300	250	200	150	100	70	50	30	20	10
Thickness (hPa)	37.5	75	112.5	125	100	100	100	75	50	50	50	40	25	20	15	10	15

simulation of TCs is found to show dependence on other aspects of model configurations such as convective parameterizations (Murakami et al. 2012; Zhao et al. 2012; Duvel et al. 2017).

With advances in computational power, it is possible to study TCs simulated in relatively high-resolution GCMs (Zhao et al. 2009; Wehner et al. 2015; Murakami et al. 2018; Vecchi et al. 2019). However, simply increasing model resolution does not necessarily improve the simulation of TC climatology. For example, Shaevitz et al. (2014) showed that high-resolution GCMs have trouble in simulating the most intense storms. In addition, while the simulated TC frequency is improved by increasing model resolution, the intensity of the simulated TCs measured by 10-m wind speed remains weak (Roberts et al. 2015). Wing et al. (2019) applied the column-integrated budget analysis to TCs simulated in high-resolution GCMs and showed that models with more intense TCs have stronger surface flux feedback. These results highlight the importance of interactions between different variables in modulating TC frequency and intensity in numerical simulations.

However, the column-integrated MSE variance budget equation cannot elucidate vertical structures of interactions between radiation, circulation, and other state variables (e.g., water vapor). Recently, Yao et al. (2021) proposed two vertically resolved (VR) MSE frameworks in which physical processes associated with convective self-aggregation can be quantified at each individual level. One focuses on the impact of diabatic/adiabatic processes on the local MSE (LMSE) variance at each level, which is referred to as the VR-LMSE framework. The other focuses on the impact of diabatic/adiabatic processes on the column-integrated MSE variance (i.e., the global MSE variance), which is referred to as the VR-GMSE framework. Yao and Yang (2021) also proposed to apply the VR MSE diagnosis to the development of TCs.

In this study, we use the VR frameworks to study TCs simulated in a high-resolution GCM with realistic boundary conditions. Interactions between radiation, moisture, and circulation are quantified at each individual pressure level for different TC intensities. Mechanism-denial experiments are conducted to compare the relative importance of radiative interactions in the boundary layer with those in the free troposphere on the global TC climatology. In addition, we explicitly compute the advection term using instantaneous 6-hourly model outputs and discuss its role in the development of TCs in this GCM.

2. Methods

a. Model and tracking TCs

The High Resolution Atmospheric Model (HiRAM) developed at the Geophysical Fluid Dynamics Laboratory (GFDL) is used in this study. HiRAM has a horizontal grid spacing of ~50 km and 32 vertical levels. HiRAM can reproduce the observed global TC climatology and interannual variability (Zhao et al. 2009). TCs simulated in this model are tracked by a method developed by Harris et al. (2016). This method uses instantaneous 6-hourly outputs of sea level pressure, midtropospheric temperature, 850-hPa vorticity, and 10-m zonal and meridional winds to track high cyclonic vorticity features. Typically, the high cyclonic vorticity is accompanied by a sea level pressure minimum, a warm core in the middle troposphere, and strong near-surface winds. The threshold regarding 10-m maximum wind speed is set as 15.3 m s^{-1}, which is suggested by Walsh et al. (2007), in which a threshold of 10% below gale force (17 m s^{-1}) for models with ~50-km horizontal grid spacing. Note that the 15.3 m s^{-1} threshold refers to a TC's maximum lifetime intensity. In other words, there are

TABLE 2. A comparison of the radiative feedback and the advection term between the VI-GMSE, VR-LMSE, and VR-GMSE frameworks in HiRAM.

	VI-GMSE variance modified from Wing and Emanuel (2014)	VR-LMSE variance modified from Yao et al. (2021)	VR-GMSE variance modified from Yao et al. (2021)
Radiative feedback	$\mathrm{GMSE}' \times \left(\sum_{i=1}^{17} R_i\right)'$, not vertically resolved	$\mathrm{LMSE}_i' \times R_i'$, $i = 1, 2, \ldots, 17$	$\mathrm{GMSE}' \times R_i'$, $i = 1, 2, \ldots, 17$
The horizontal component of the advection term	$-\mathrm{GMSE}' \times \left(\sum_{i=1}^{17}\left[\frac{\partial(u_i \times \mathrm{LMSE}_i)}{\partial x} + \frac{\partial(v_i \times \mathrm{LMSE}_i)}{\partial y}\right]\right)'$	$-\mathrm{LMSE}_i' \times \left[\frac{\partial(u_i \times \mathrm{LMSE}_i)}{\partial x} + \frac{\partial(v_i \times \mathrm{LMSE}_i)}{\partial y}\right]'$, $i = 1, 2, \ldots, 17$	$-\mathrm{GMSE}' \times \left[\frac{\partial(u_i \times \mathrm{LMSE}_i)}{\partial x} + \frac{\partial(v_i \times \mathrm{LMSE}_i)}{\partial y}\right]'$, $i = 1, 2, \ldots, 17$
The vertical component of the advection term	—	$-\mathrm{LMSE}_i' \times \left[\frac{\partial(\omega_i \times \mathrm{LMSE}_i)}{\partial p}\right]'$, $i = 1, 2, \ldots, 17$	$-\mathrm{GMSE}' \times \left[\frac{\partial(\omega_i \times \mathrm{LMSE}_i)}{\partial p}\right]'$, $i = 1, 2, \ldots, 17$

Brought to you by NOAA Central Library | Unauthenticated | Downloaded 01/30/24 02:51 PM UTC

TABLE 3. A list of the simulations in this study.

Experiment name	SST forcing	CO_2 forcing	Radiation
Control	1986–2005 average	Fixed	Fully interactive
ClimRad	1986–2005 average	Fixed	Prescribed climatology
ClimRadFT	1986–2005 average	Fixed	Prescribed climatology in the free troposphere, fully interactive in the boundary layer (see section 3b and Table 4)
ClimRadBL	1986–2005 average	Fixed	Prescribed climatology in the boundary layer, fully interactive in the free troposphere (see section 3b and Table 4)

time steps when a TC's intensity is smaller than 15.3 m s^{-1} throughout its lifetime. In addition, we set the minimum warm core temperature anomaly relative to the surrounding environment at 2.5 K to yield comparable global-mean TC frequency as observations. The tracked TCs are categorized into two groups: (i) the first group includes tropical storms (category 0) through category 5 hurricanes, which is referred to as category 0–5 TCs. The threshold of 10-m maximum wind speed is 15.3 m s^{-1}. (ii) The second group includes category 1 to category 5 TCs with the threshold set as 29.3 m s^{-1}. This group is referred to as category 1–5 TCs.

b. *Vertically resolved frameworks*

MSE (denoted as h) is defined as

$$h = c_p T + gz + L_v q, \tag{1}$$

where c_p is the specific heat of dry air, T is the air temperature, g is the gravitational acceleration, z is the height above the surface, L_v is the latent heat of vaporization, and q is the specific humidity. The budget for the vertically integrated MSE (denoted as $\hat{h}$) is computed as

$$\frac{\partial \hat{h}}{\partial t} = \mathrm{THF} + R - \nabla_h \cdot \widehat{\mathbf{u}h}, \tag{2}$$

where THF is the surface turbulent heat flux including latent and sensible heat flux, R is the net radiation of the atmosphere including both shortwave (SW) and longwave (LW) components, and $-\nabla_h \cdot \widehat{\mathbf{u}h}$ is the horizontal convergence of the vertically integrated flux of h. Here, Eq. (2) is based on pressure coordinates and thus has a simplified continuity equation.

Wing and Emanuel (2014) introduced a budget equation for the spatial variance of horizontal anomalies of vertically integrated MSE (denoted as $\hat{h}'$):

$$\frac{1}{2}\frac{\partial(\hat{h}'^2)}{\partial t} = \hat{h}' \times \mathrm{THF}' + \hat{h}' \times R' - \hat{h}' \times (\nabla_h \cdot \widehat{\mathbf{u}h})', \tag{3}$$

where $\hat{h}' \times \mathrm{THF}'$ represents the surface flux feedback, $\hat{h}' \times R'$ is the radiative feedback, and $-\hat{h}' \times (\nabla_h \cdot \widehat{\mathbf{u}h})'$ is the advection term. As illustrated in Yao et al. (2021), this framework includes (i) the local MSE variance at a given vertical level and (ii) the covariance of MSE anomalies between different vertical levels. They refer to this framework as the global MSE (GMSE) variance framework.

The vertically integrated GMSE (VI-GMSE) variance framework [Eq. (3)] does not show the vertical distribution of interaction between variables that is important to the deep convective system (Mapes 2016). Previous studies argued that physical processes in the boundary layer play a key role in convective aggregation (Jeevanjee and Romps 2013; Muller and Bony 2015; Yang 2018b,a). To resolve the vertical dimension, Yao et al. (2021) proposed a set of VR analyses. Such analyses focus on either local MSE variance (referred to as the VR-LMSE variance framework) or global MSE variance (referred to as the VR-GMSE variance framework). LMSE is defined at a specific pressure level [Eq. (5)], whereas GMSE is integrated over the entire atmospheric column [Eq. (6)]. These two frameworks shed light on the vertical distributions of interactions between radiation, circulation, and MSE. More details can be found in section 3 of Yao et al. (2021).

Here, we follow the VR approach to investigate the vertical distribution of interactions between radiation, circulation, and MSE associated with TCs simulated in HiRAM. The original model output on 32 sigma levels is interpolated to standard pressure levels from 1000 to 10 hPa with 17 vertical pressure levels in total. Variables can be quantified at each individual pressure level. Table 1 lists values of the pressure levels and their thickness. Here, we use the model-generated, four-dimensional, instantaneous, 6-hourly outputs.

The net radiation at each individual pressure level (i.e., radiative flux divergence, denoted as R_i with a unit of W m^{-2} where i is the level index) is computed by radiative cooling rates (denoted as tdt_i with a unit of K s^{-1}):

$$R_i = \frac{C_p}{g} \times \mathrm{tdt}_i \times \Delta p_i, \tag{4}$$

and the density-weighted LMSE at level i (with a unit of J m^{-2}) is computed as

TABLE 4. Radiation in the ClimRadFT run and the ClimRadBL run. The term tdt_M represents model-generated radiative cooling rates while tdt_C is climatological radiative cooling rates computed from the Control run. There are 32 vertical levels in HiRAM. Level 1 is the top level and level 32 is the bottom level.

	ClimRadFT	ClimRadBL
Levels 1–21	Prescribed (tdt_C)	Fully interactive (tdt_M)
Level 22	$0.2 \times \mathrm{tdt}_M + 0.8 \times \mathrm{tdt}_C$	$0.8 \times \mathrm{tdt}_M + 0.2 \times \mathrm{tdt}_C$
Level 23	$0.4 \times \mathrm{tdt}_M + 0.6 \times \mathrm{tdt}_C$	$0.6 \times \mathrm{tdt}_M + 0.4 \times \mathrm{tdt}_C$
Level 24	$0.6 \times \mathrm{tdt}_M + 0.4 \times \mathrm{tdt}_C$	$0.4 \times \mathrm{tdt}_M + 0.6 \times \mathrm{tdt}_C$
Level 25	$0.8 \times \mathrm{tdt}_M + 0.2 \times \mathrm{tdt}_C$	$0.2 \times \mathrm{tdt}_M + 0.8 \times \mathrm{tdt}_C$
Levels 26–32	Fully interactive (tdt_M)	Prescribed (tdt_C)

Brought to you by NOAA Central Library | Unauthenticated | Downloaded 01/30/24 02:51 PM UTC

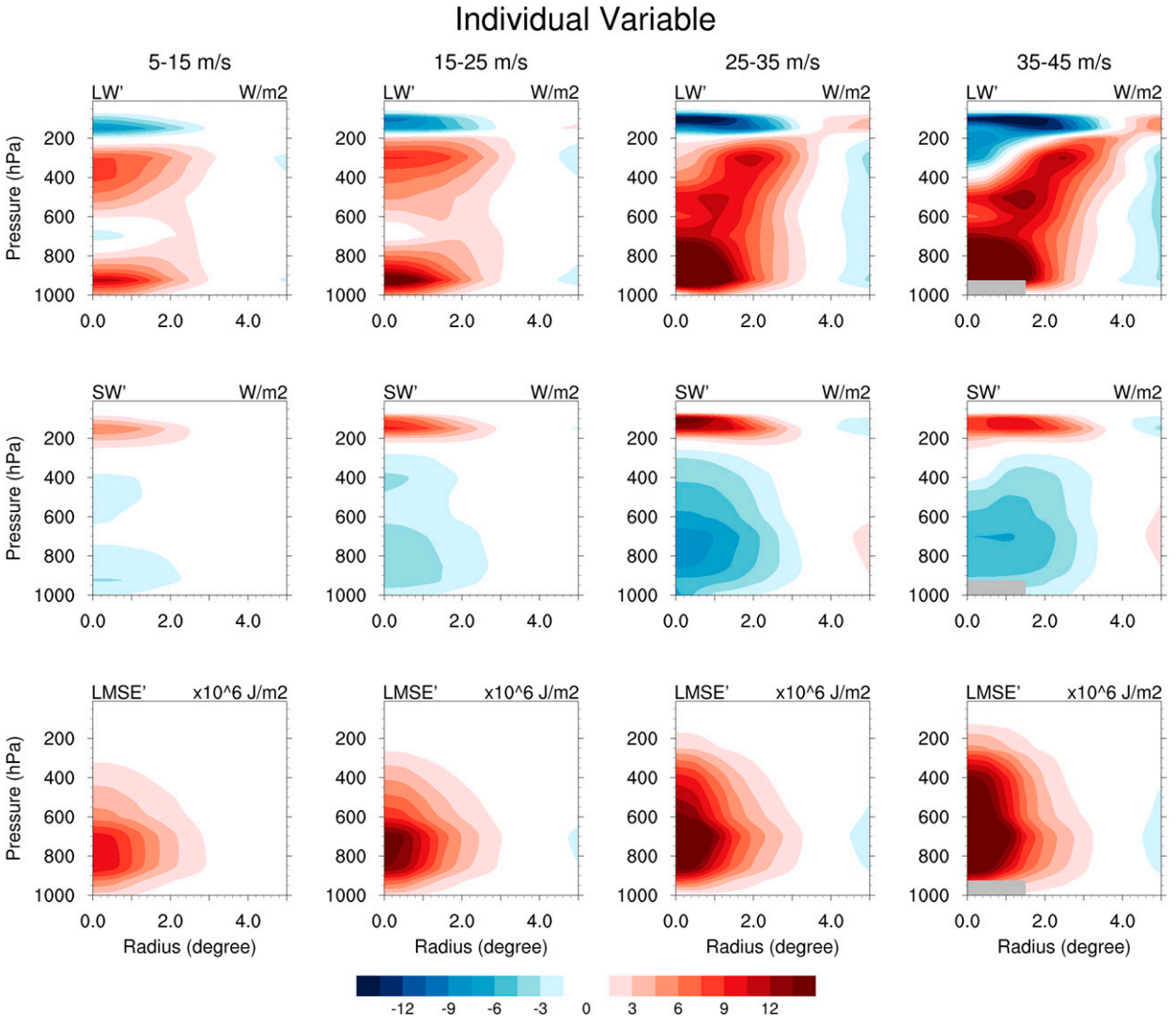

FIG. 1. (top) Vertical cross sections of azimuthally averaged and density-weighted individual variables for the LW component of R_i' (W m^{-2}), (middle) SW component of R_i' (W m^{-2}), and (bottom) LMSE$_i'$ (1×10^6 J m^{-2}) during different TC intensities: 5–15, 15–25, 25–35, and 35–45 m s^{-1} with the sample size being 833, 2886, 1021, and 170, respectively, from left to right. Missing values are in gray shadings.

$$\mathrm{LMSE}_i = \frac{1}{g} \times h_i \times \Delta p_i, \tag{5}$$

where Δp_i is the pressure thickness for the ith pressure level (Table 1). GMSE is computed as

$$\mathrm{GMSE} = \sum_{i=1}^{17} \mathrm{LMSE}_i. \tag{6}$$

For each variable at pressure level i, we consider a $\sim 10^\circ \times 10^\circ$ box centered on the tracked TCs. Within the box, anomalies of each variable at each grid point are computed by removing its domain average of the $\sim 10^\circ \times 10^\circ$ box. We use the prime symbol to represent anomalies of variables. In the VR-LMSE framework, $\mathrm{LMSE}_i' \times R_i'$ represents the radiative feedback at pressure level i. For the advection term at pressure level i, $-\mathrm{LMSE}_i' \times \{[\partial(u_i \times \mathrm{LMSE}_i)/\partial x] + [\partial(v_i \times \mathrm{LMSE}_i)/\partial y]\}'$ is the horizontal component, where u_i and v_i are zonal and meridional wind (m s^{-1}), $-\mathrm{LMSE}_i' \times [\partial(\omega_i \times \mathrm{LMSE}_i)/\partial p]'$ is the vertical component, where ω_i is the vertical wind component (Pa s^{-1}). The vertical component includes convective transport that is not explicitly present in the VI-GMSE framework. This could to some extent complicate the interpretation of the advection term in the VR-LMSE framework. We also consider the VR-GMSE framework, in which $\mathrm{GMSE}' \times R_i'$ represents the radiative feedback at pressure level i (note that vertical integration is done first before removing its domain average to get GMSE′). The advection term at pressure level i in the VR-GMSE framework is $-\mathrm{GMSE}' \times \{[\partial(u_i \times \mathrm{LMSE}_i)/\partial x] + [\partial(v_i \times \mathrm{LMSE}_i)/\partial y]\}'$ for the horizontal component and $-\mathrm{GMSE}' \times [\partial(\omega_i \times \mathrm{LMSE}_i)/\partial p]'$ for the vertical component. The radiative feedback and the advection

Brought to you by NOAA Central Library | Unauthenticated | Downloaded 01/30/24 02:51 PM UTC

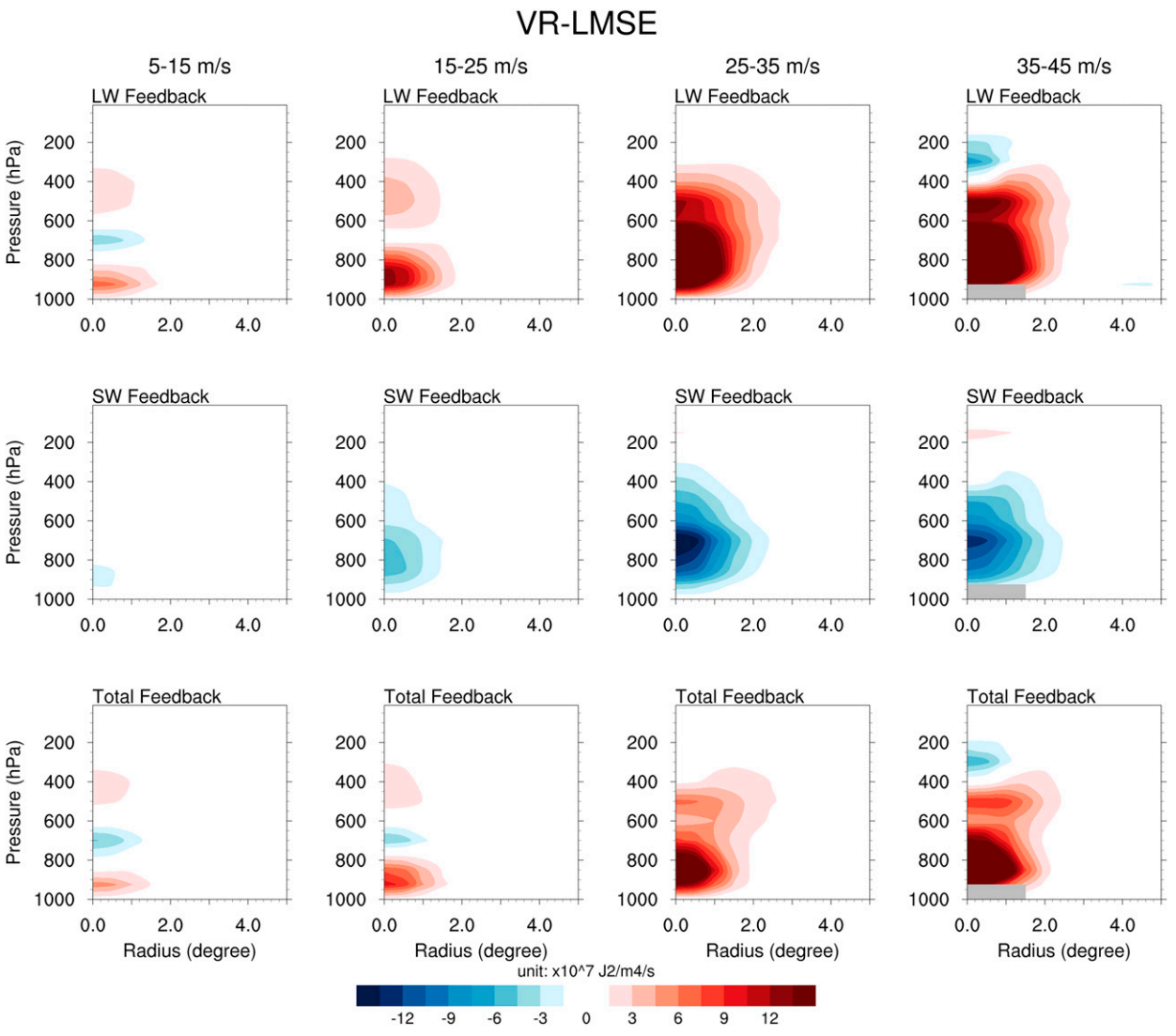

FIG. 2. As in Fig. 1, but for the (top) LW component, (middle) SW component, and (bottom) the total (LW + SW) of $\mathrm{LMSE}_i' \times R_i'$ (units are 1×10^7 J^2 m^{-4} s^{-1}).

term computed in the VI-GMSE, VR-LMSE, and VR-GMSE frameworks are listed in Table 2.

c. *Experiments*

All simulations in this study are performed with prescribed climatological monthly means of sea surface temperatures and sea ice from the Hadley Centre Sea Ice and Sea Surface Temperature dataset (HadISST; Rayner et al. 2003) based on the 20-yr period from 1986 to 2005 and a constant atmospheric CO_2 concentration at 1990 levels. We first have a simulation that is integrated for 50 years with the default model configuration and fully interactive radiation (referred to as the Control run). To assess the relative importance of radiative interactions at different levels of the atmosphere, we perform two mechanism-denial experiments: one simulation has suppressed radiative interactions in the boundary layer but interactive radiation in the free troposphere (referred to as the ClimRadBL run); the other simulation has interactive radiation in the boundary layer but suppressed radiative interactions in the free troposphere (referred to as the ClimRadFT run). Suppressed radiative interactions means that model-generated atmospheric radiative cooling rates at each time step are overwritten by their monthly varying climatological values computed from the Control simulation. Note that both the total radiative interactions including both the longwave and shortwave components are considered in these experiments. Another mechanism-denial experiment in which radiative interactions are entirely suppressed (referred to as the ClimRad run) is added here for reference (Zhang et al. 2021a). Other aspects of these experiments can be found in Zhang et al. (2021b). Table 3 lists the simulations used in this study.

In HiRAM, the bottom 7 levels (level 26 to level 32) generally account for space from surface to ~850-hPa pressure level. Radiative cooling rates (including both longwave and

Brought to you by NOAA Central Library | Unauthenticated | Downloaded 01/30/24 02:51 PM UTC

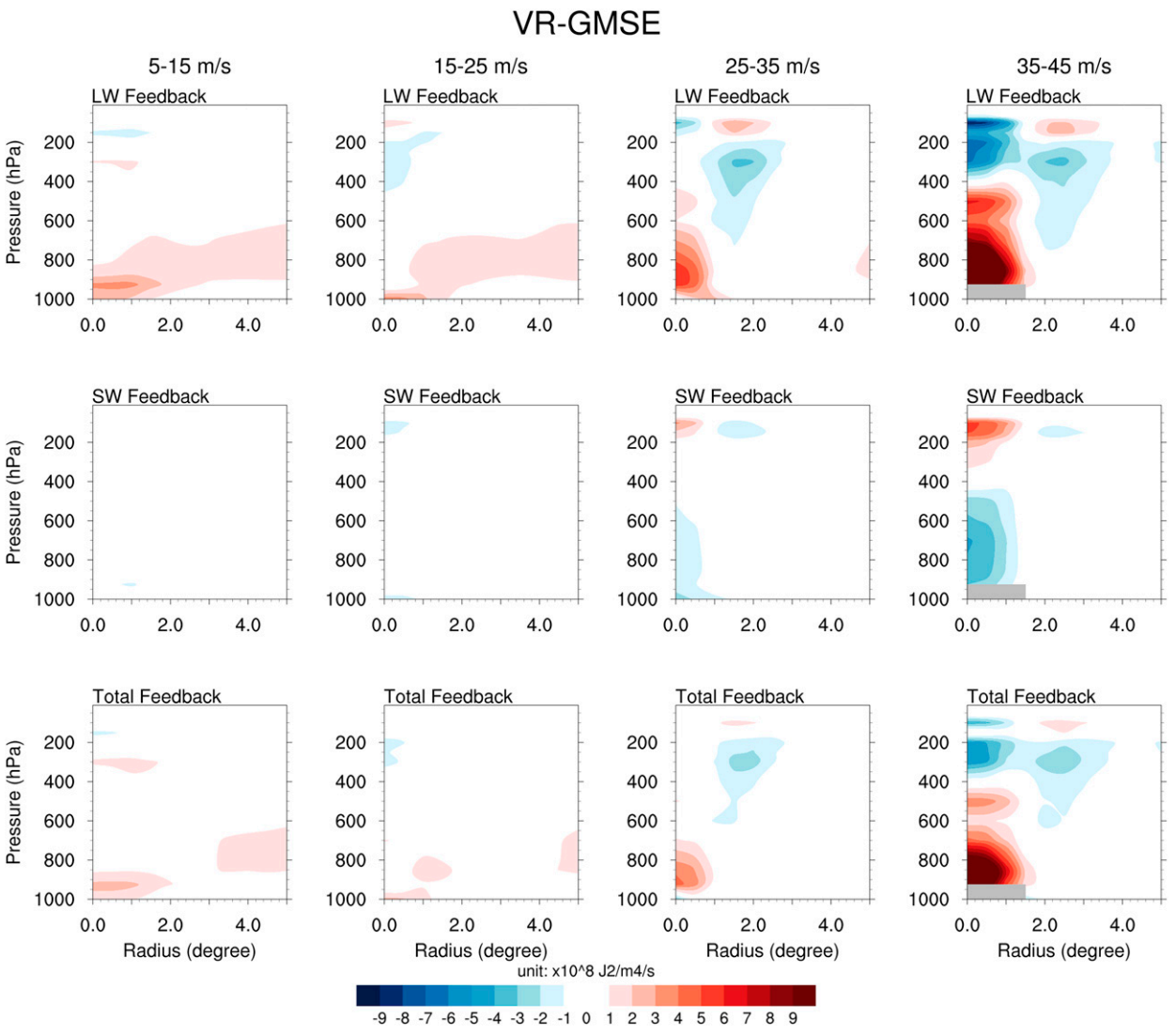

FIG. 3. As in Fig. 1, but for the (top) LW component, (middle) SW component, and (bottom) the total (LW + SW) of GMSE′ × R_i' (units are 1×10^8 J^2 m^{-4} s^{-1}).

shortwave) in the ClimRadBL run are fixed from level 26 to level 32 and linearly transition to fully interactive at level 21 (~700 hPa), which means that radiative cooling rates at level 21 consist of 100% of model-generated values. Radiative cooling rates in the ClimRadFT run are the other way around in which radiative cooling rates are fully interactive from level 26 to level 32 and linearly transition to fully fixed values at level 21. Table 4 illustrates details of how radiative cooling rates are configured in the ClimRadFT and ClimRadBL runs.

3. Results

a. Radiative production

Figure 1 shows vertical cross sections of the LW and SW components of R_i' and LMSE$_i'$ averaged azimuthally during different TC intensities from the 5–15 m s^{-1} bin to the 35–45 m s^{-1} bin. Positive values of R_i' mean anomalous heating at pressure level i to the domain average, while negative ones mean anomalous cooling to the domain average. For the LW component, positive anomalies dominate the atmospheric column from the surface to ~200 hPa, whereas negative ones are found in the upper troposphere. The SW component exhibits opposite profiles in general. Similar structures of R_i' associated with TCs are also discernable from satellite observations (Feng and Huang 2021). Unlike the vertically varied radiative responses, positive anomalies of LMSE$_i'$ dominate the troposphere.

We further our analyses by investigating the vertical structure of interactions between R_i' and LMSE$_i'$ in the VR-LMSE framework. Figure 2 shows vertical cross sections of the LW and SW components of LMSE$_i'$ × R_i'. Positive values of LMSE$_i'$ × R_i' indicate positive feedback at pressure level i, which is thought to increase local MSE variance. Negative values do the opposite and thus decrease local MSE variance.

Brought to you by NOAA Central Library | Unauthenticated | Downloaded 01/30/24 02:51 PM UTC

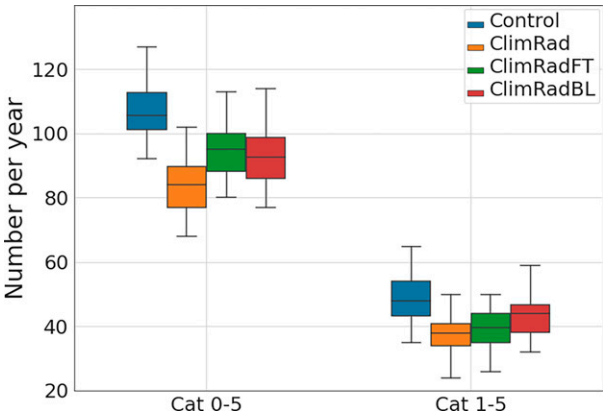

FIG. 4. Boxplots of the global number of TCs per year for category 0–5 and category 1–5 TCs for the Control run (blue), ClimRad run (orange), ClimRadFT run (green), and ClimRadBL run (red).

The results in Fig. 2 indicate that the LW feedback is mainly positive and promotes the development of TCs, while the SW feedback is negative and inhibits it. However, the total radiative feedback is positive because the magnitude of SW feedback is smaller than that of the LW feedback. Overall, these results are consistent with previous studies on TCs simulated in convection-resolving models (Wing et al. 2016; Muller and Romps 2018; Ruppert et al. 2020; Wu et al. 2021). Although the magnitude of perturbation in SW radiation associated with TCs is small, the SW component of $\mathrm{LMSE}_i' \times R_i'$ is negative and counteracts the diabatic contribution from the LW component. However, the SW feedback in the VI-GMSE framework is almost negligible compared to the other terms (Wing et al. 2016; Muller and Romps 2018; Zhang et al. 2021a). One primary reason is that opposing changes in SW radiation at different pressure levels tend to cancel out when vertically integrated. As a result, the impact of the SW feedback can be largely neglected in the VI-GMSE framework.

Compared to the VR-LMSE framework, the VR-GMSE framework focuses on vertically integrated MSE anomalies but retains profiles of other variables such as radiation. Figure 3 shows vertical cross sections of the LW and SW components of $\mathrm{GMSE}' \times R_i'$. The term $\mathrm{GMSE}' \times R_i'$ can be expanded as $(\mathrm{LMSE}_1 + \mathrm{LMSE}_2 + \cdots + \mathrm{LMSE}_{17})' \times R_i'$. However, note that $(\mathrm{LMSE}_1 + \mathrm{LMSE}_2 + \cdots + \mathrm{LMSE}_{17})' \neq (\mathrm{LMSE}_1' + \mathrm{LMSE}_2' + \cdots + \mathrm{LMSE}_{17}')$ because the domain average of LMSE is not a constant but varies with height. In general, the radiative feedbacks

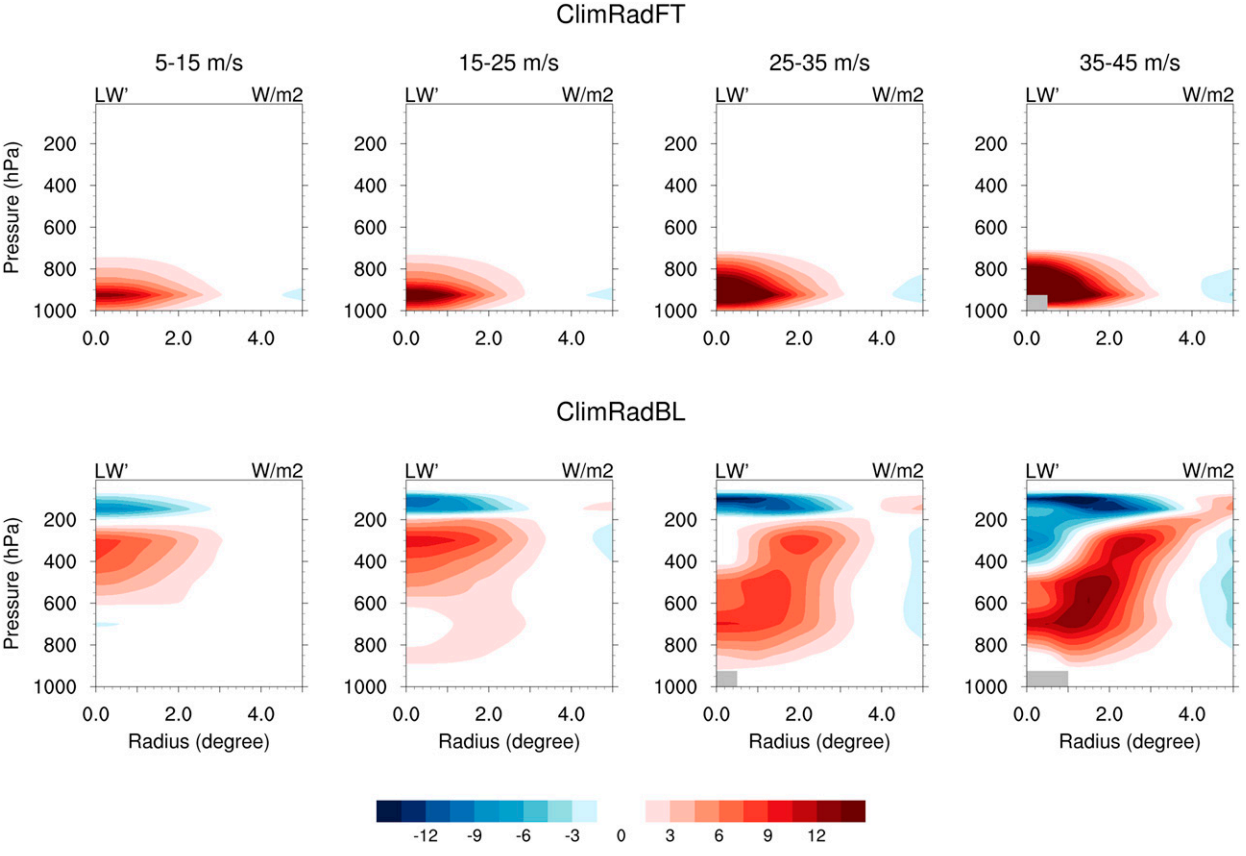

FIG. 5. Vertical cross sections of azimuthally averaged and density-weighted LW component of R_i' in the (top) ClimRadFT run and the (bottom) ClimRadBL run during different TC intensities: 5–15, 15–25, 25–35, and 35–45 m s^{-1}. The sample size for the ClimRadFT run is 687, 2026, 715, and 137, respectively, from left to right, and that for the ClimRadBL run is 688, 2118, 843, and 259. Missing values are in gray shadings.

Brought to you by NOAA Central Library | Unauthenticated | Downloaded 01/30/24 02:51 PM UTC

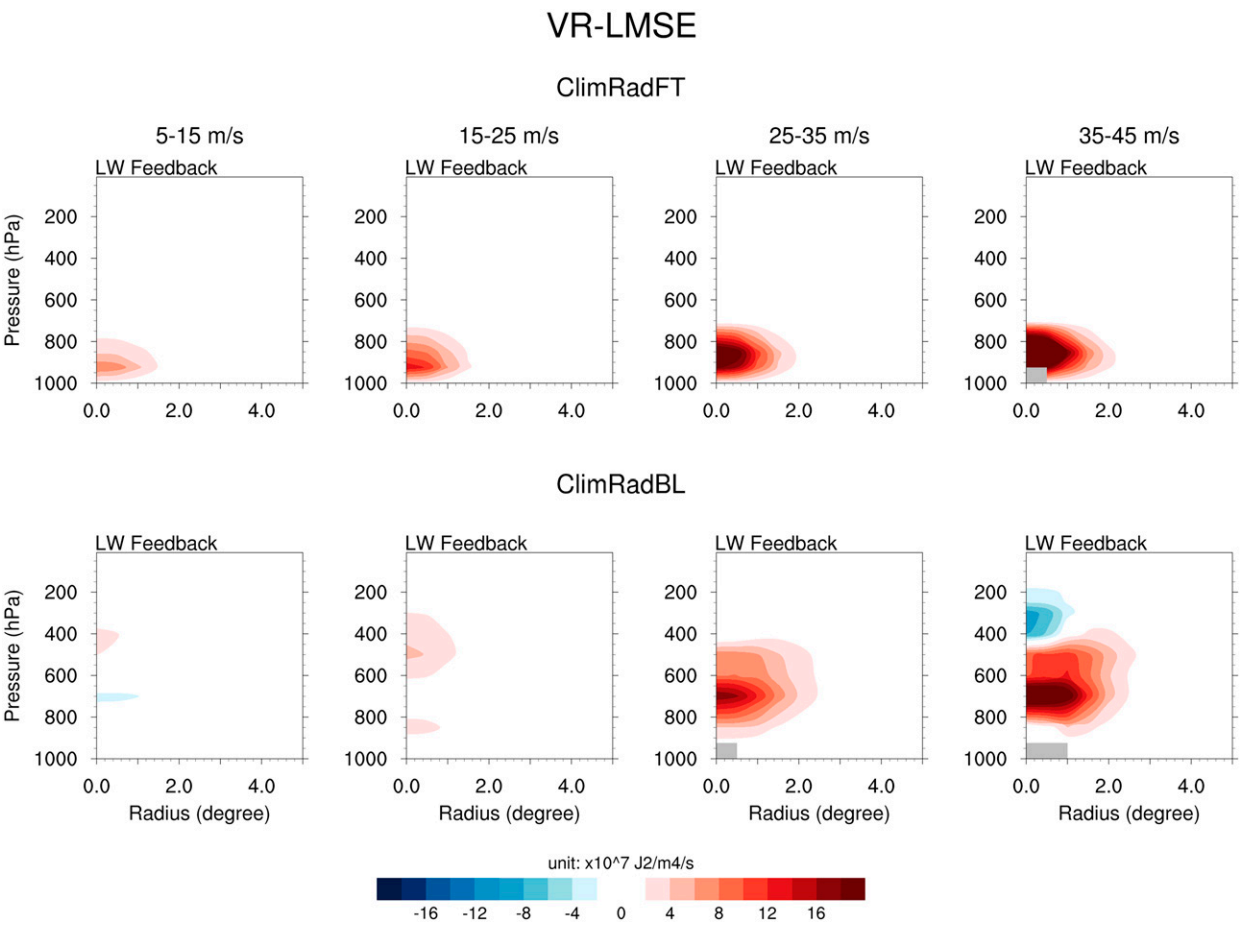

FIG. 6. As in Fig. 5, but for the LW component of $\mathrm{LMSE}_i' \times R_i'$ (units are 1×10^7 J^2 m^{-4} s^{-1}).

in the VR-GMSE framework qualitatively resemble those in the VR-LMSE framework. However, in the VR-GMSE framework, R_i' is multiplied with GMSE′, which introduces extra covariance terms that are not considered in the VR-LMSE framework (Yao et al. 2021) and thus leads to overall greater values in the VR-GMSE framework (more comparisons can be found later in Fig. 8).

b. *Partly removing radiative production*

In HiRAM, Zhang et al. (2021a) showed that the global number of TCs per year is reduced by ~20% when synoptic-scale radiative interactions are suppressed by prescribing climatological radiative heating rates. Given the vertically varied contribution of $\mathrm{LMSE}_i' \times R_i'$ to the development of TCs (Fig. 2), we now explore how global TC frequency would be affected when synoptic-scale radiative interactions associated with TCs are partly suppressed. Specifically, we compare the role of radiative coupling in the boundary layer with that in the free troposphere. To do that, we examine responses of TCs in the ClimRadFT and ClimRadBL runs (section 2c). The results from the ClimRad run in which radiative interactions are entirely suppressed (Zhang et al. 2021a) is added here for reference.

Figure 4 shows the global number of TCs per year in the Control, ClimRad, ClimRadFT, and ClimRadBL runs. Compared to the Control run, the global number of TCs per year exhibits an overall reduction when radiative interactions are suppressed, which reflects the positive radiative production of LMSE variance in the development of TCs. However, the magnitude of reduction varies between these simulations. In general, the ClimRad run exhibits the largest reduction, while the reduction in the ClimRadFT run and the ClimRadBL run are smaller, indicating that partly suppressing radiative interactions is less effective in reducing global TC frequency than entirely suppressing radiative interactions.

We note that the surface fluxes are set as default in these mechanism-denial experiments, which makes the surface flux feedback similar between these experiments in which more intense TCs exhibit greater positive surface flux feedback (Wing et al. 2019; Zhang et al. 2021a). The positive surface flux feedback is consistent with the results found in convection-resolving models (Wing et al. 2016; Muller and Romps 2018), reflecting robust wind-induced surface heat exchange (WISHE) feedback associated with TCs. However, the surface flux feedback can be negative for general convective aggregation (Wing and Emanuel 2014; Yao et al. 2021). This is a major difference

Brought to you by NOAA Central Library | Unauthenticated | Downloaded 01/30/24 02:51 PM UTC

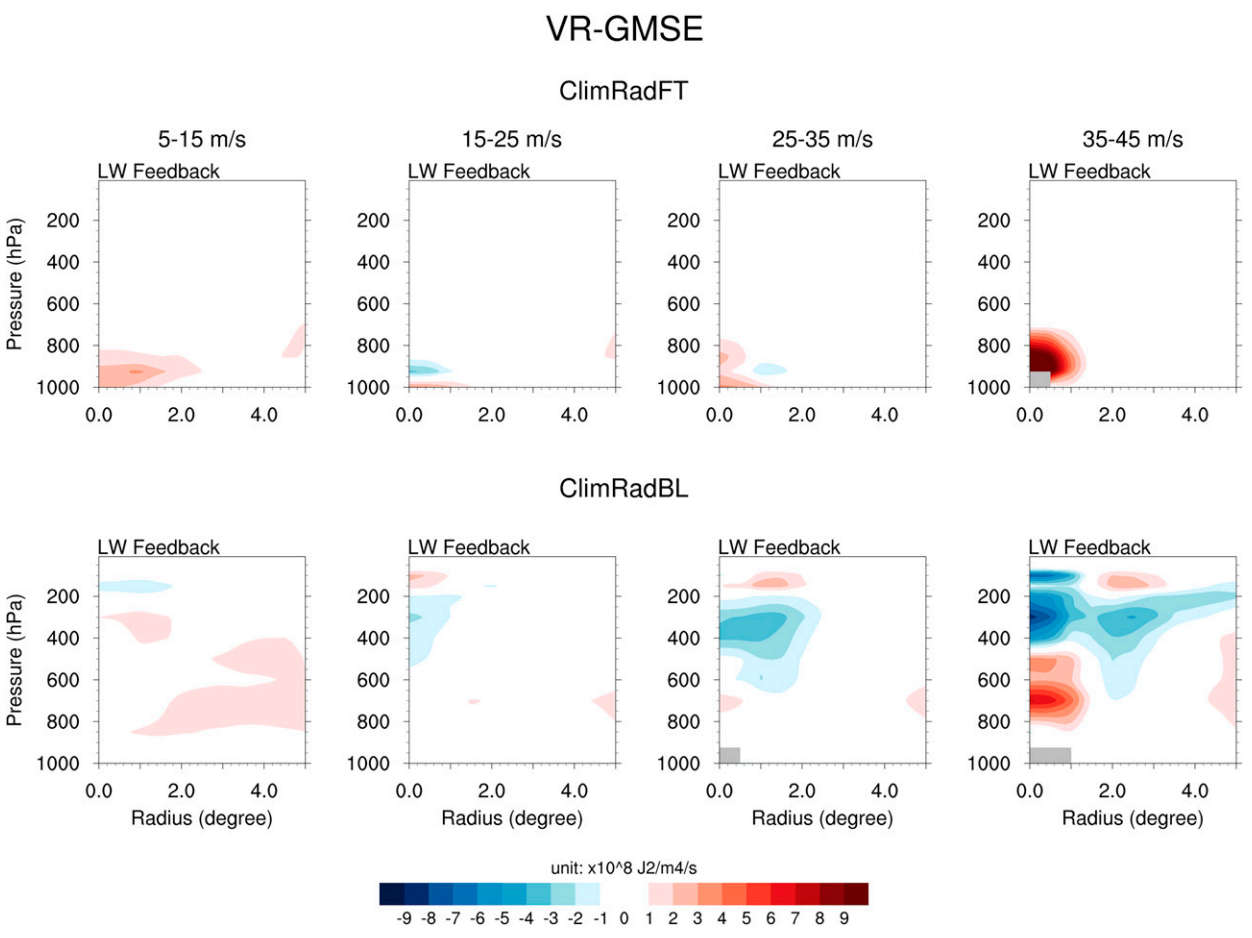

FIG. 7. As in Fig. 5, but for the LW component of GMSE′ × R_i' (units are 1×10^8 J^2 m^{-4} s^{-1}).

between TCs and convective aggregation. Given the similar behaviors of the surface flux feedback among these experiments, we focus on other terms for the budget analysis in the remainder of this paper.

When radiative interactions are partly suppressed, the overall reduction in global TC frequency can be understood by the vertical profile of R_i', LMSE$_i'$ × R_i', and GMSE′ × R_i' in the ClimRadFT and ClimRadBL runs. Here, we focus on the LW component of these variables. In the ClimRadFT run, positive values of R_i' are found mainly below ~800 hPa but are negligible in the free troposphere (Fig. 5, the first row). In the ClimRadBL run, the response of radiation in the boundary layer is nearly zero. Positive values of R_i' are found mainly in the free troposphere, whereas negative ones are found from ~200 hPa and above (Fig. 5, the second row). The profiles of LMSE$_i'$ × R_i' largely resemble the vertical distribution of R_i' as shown in Fig. 5. In the ClimRadFT run, the contribution of the LW feedback to LMSE variance is negligible in the free troposphere but is robust in the boundary layer (Fig. 6, the first row). In the ClimRadBL run, the contribution is significant in the free troposphere but is largely missing in the boundary layer (Fig. 6, the second row). However, we note that the profiles of GMSE′ × R_i' are less coherent spatially. There are more spatial variations for GMSE′ × R_i', especially in the small intensity bins (Fig. 7). According to Eq. (7), GMSE is computed as a density-weighted integration of LMSE. Still, GMSE′ × R_i' can be written as (LMSE$_1$ + LMSE$_2$ + ⋯ + LMSE$_{17}$)′ × R_i', which involves covariance terms (Yao et al. 2021). These covariance terms lead to the difference between Figs. 6 and 7.

Compared to the profiles of LMSE$_i'$ × R_i' in which the impact of local radiation on local MSE is considered, GMSE′ × R_i' include the contribution from the covariance terms that lack a sound physical explanation (Yao et al. 2021). The VR-LMSE framework tends to shed light on "local processes," while the VR-GMSE framework tends to evaluate the impact of local diabatic process on the column-integrated system. Here, it seems that the analyses using the VR-LMSE framework, in which the covariance terms are excluded, provide a cleaner picture of the vertically varied

TABLE 5. Fractional change in the global number of TCs per year in the ClimRad run, ClimRadFT run and ClimRadBL run in comparison to the Control run.

	ClimRad	ClimRadFT	ClimRadBL
Category 0–5	22.0%	12.1%	13.1%
Category 1–5	23.0%	18.5%	10.4%

Brought to you by NOAA Central Library | Unauthenticated | Downloaded 01/30/24 02:51 PM UTC

TABLE 6. Ratio of the global number of category 0–5 TCs per year to the global number of category 1–5 TCs per year in the Control run, ClimRad run, ClimRadFT run, and ClimRadBL run.

	Control	ClimRad	ClimRadFT	ClimRadBL
ratio = $\frac{\text{category 0–5}}{\text{category 1–5}}$	2.211	2.240	2.385	2.144

contribution of the radiative feedback among these mechanism-denial experiments. However, more research is required to understand the remote impact and thus the covariance terms before the analyses related to GMSE are given more credit.

In terms of the VI analysis related to LMSE, the total amount of $\text{LMSE}'_i \times R'_i$ in the ClimRadFT and ClimRadBL runs are greater than that in the ClimRad run (which is almost zero) but smaller than that in the Control run (Fig. 8). These results, to some extent, explain the smaller reduction in global TC frequency in the ClimRadFT and ClimRadBL runs compared to that in the ClimRad run. However, we note that the global TC frequency does not necessarily respond linearly to the total amount of radiative production $\text{LMSE}'_i \times R'_i$ for the VI analysis (Fig. 8). For category 0–5 TCs, the ClimRadFT run and the ClimRadBL run show a similar magnitude of reduction. However, the ClimRadFT run has a greater reduction for category 1–5 TCs than the ClimRadBL run (Fig. 4 and Table 5). Indeed, the ratio of category 0–5 TCs to category 1–5 TCs is slightly larger in the ClimRadFT run than that in the ClimRadBL run (Table 6), indicating that stronger TCs are more sensitive to radiative interactions in the free

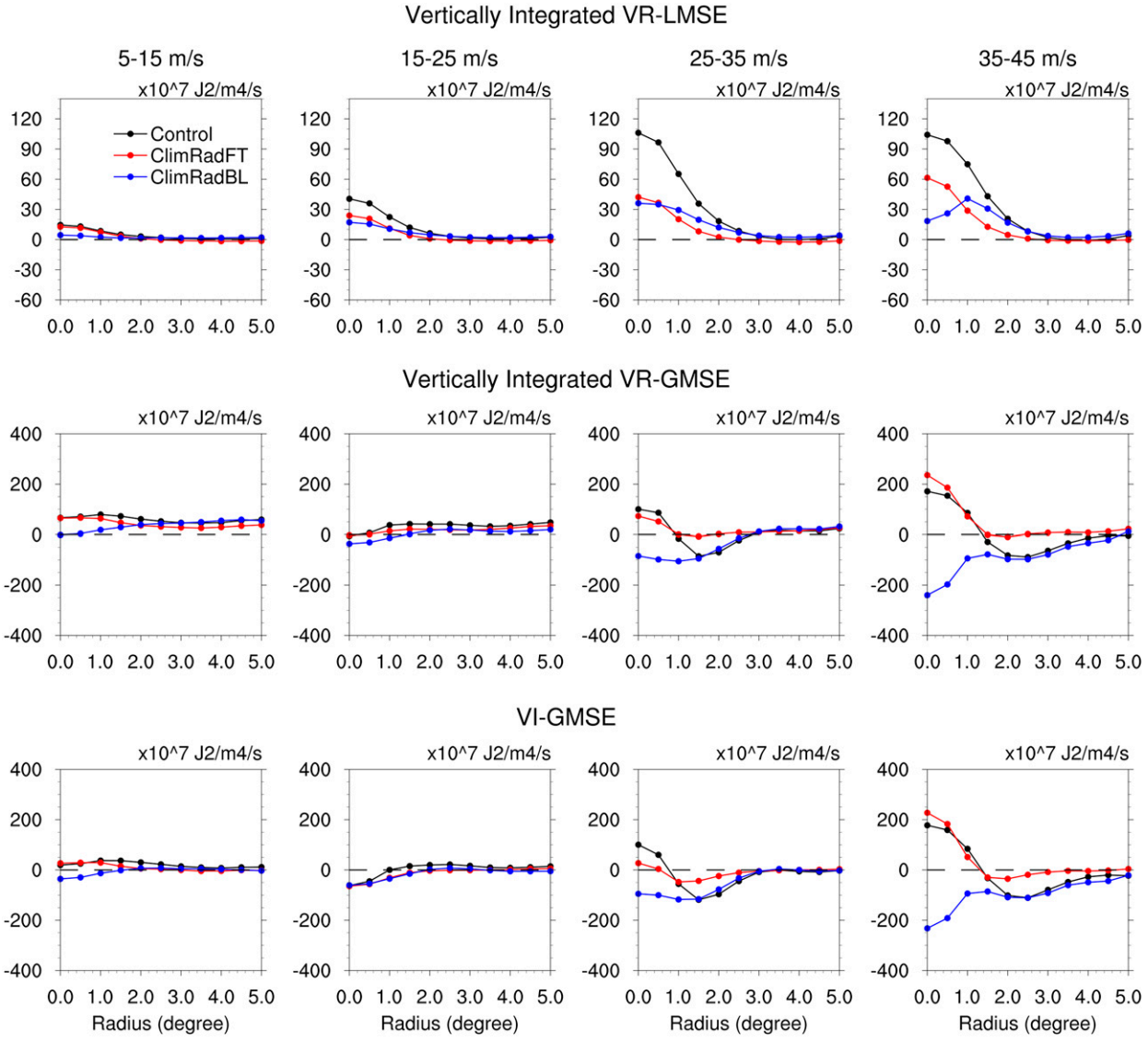

FIG. 8. The vertical integral of the LW component of $\text{LMSE}'_i \times R'_i$ in the Control run (the black lines), the ClimRadFT run (the red lines), and the ClimRadBL run (the blue lines) during different TC intensities: 5–15, 15–25, 25–35, and 35–45 m s^{-1}.

Brought to you by NOAA Central Library | Unauthenticated | Downloaded 01/30/24 02:51 PM UTC

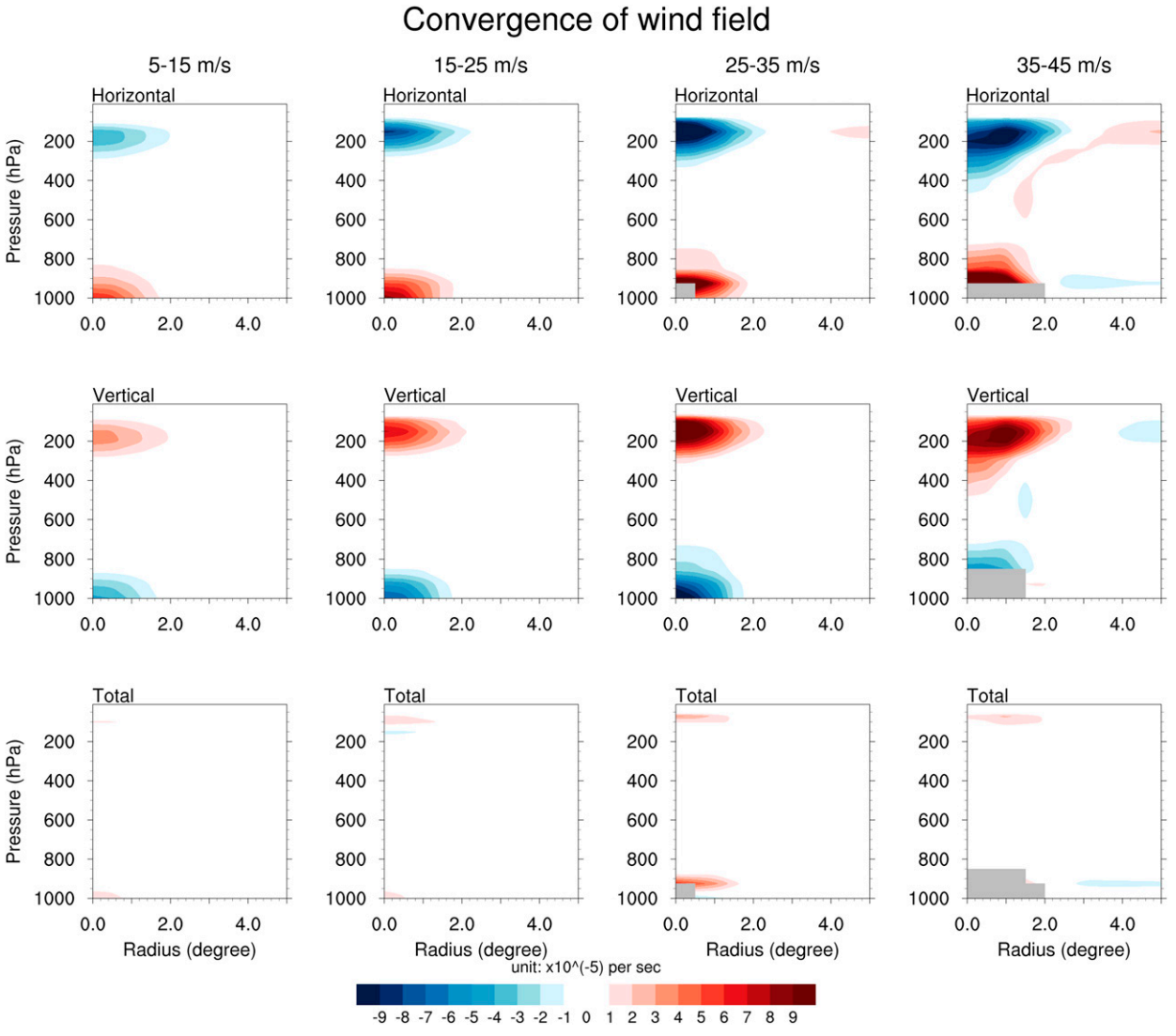

FIG. 9. As in Fig. 1, but for (top) the convergence of the horizontal wind field $-[(\partial u/\partial x) + (\partial v/\partial y)]'$, (middle) the convergence of the vertical wind field $-[\partial\omega/\partial p]'$, and (bottom) their sum (units are 1×10^{-5} s^{-1}).

troposphere. Broadly speaking, these results indicate that partly suppressing radiative interactions is less effective in reducing global TC frequency than entirely suppressing radiative interactions. In addition to examining the impact of radiative feedback from a vertically integrated perspective, the vertical distribution of radiative feedback is also important and may have different impacts on different types of TCs.

Recall that R_i' is mainly negative in the upper levels in the Control run (Fig. 1, the first row) and the ClimRadBL run (Fig. 5, the second row). However, these negative values in the upper levels are largely missing in the ClimRadFT run (Fig. 5, the first row). The presence of the negative values of R_i' in the upper levels yield negative values of GMSE$' \times R_i'$. As a result, the vertically integrated LW feedbacks in the ClimRadFT run (negative R_i' is missing) can be greater than those in the Control run for the VR-GMSE and VI-GMSE frameworks. Similarly, compared to the Control run, the ClimRadBL run retains negative values of R_i' in the upper levels but removes positive ones in the boundary layer (Fig. 5, the second row). This could even lead to negative vertically integrated LW feedbacks in the VR-GMSE and VI-GMSE frameworks (the blue lines in Fig. 8).

However, this does not indicate that the LW feedback in general opposes TC development. The profiles of R_i' in Fig. 5 and the profiles of LMSE$_i' \times R_i'$ in Fig. 6 show predominantly positive values, indicating the positive contribution from local interactions. While the frameworks related to GMSE are useful in interpreting the physical processes, the covariance terms (i.e., nonlocal interactions) involved in these frameworks need a sound explanation and thus require more research

Brought to you by NOAA Central Library | Unauthenticated | Downloaded 01/30/24 02:51 PM UTC

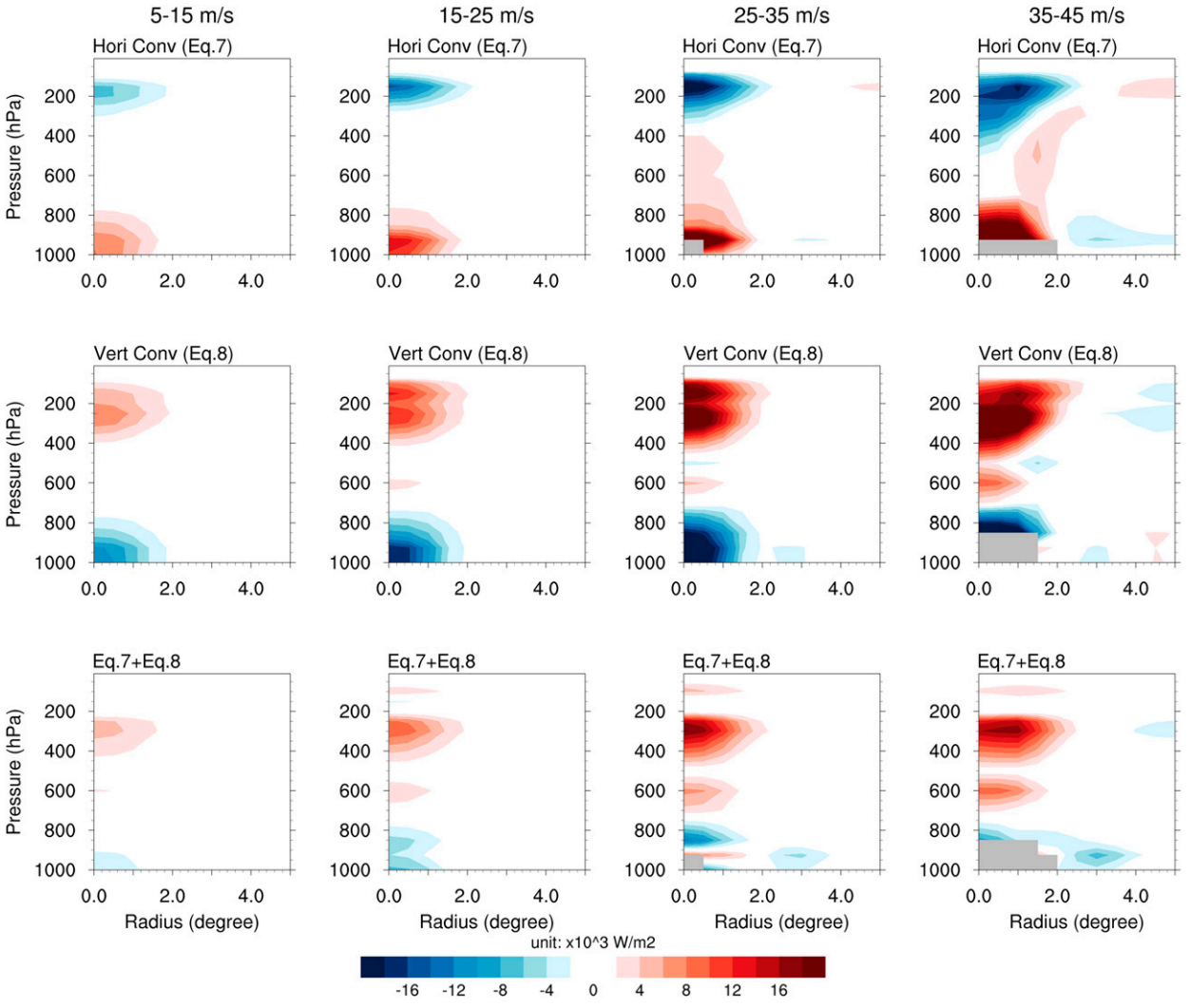

FIG. 10. As in Fig. 1, but for (top) density-weighted $-\{[\partial(u_i \times \mathrm{LMSE}_i)/\partial x] + [\partial(v_i \times \mathrm{LMSE}_i)/\partial y]\}'$ and (middle) $-[\partial(\omega_i \times \mathrm{LMSE}_i)/\partial p]'$, and (bottom) the sum of them (units are 1×10^3 W m^{-2}) in the VR-LMSE framework.

as proposed by Yao et al. (2021). The opposing results in terms of the vertically integrated values imply that only knowing the vertical integral may not be enough. The vertical profiles do provide additional and useful information, which is the main goal of this study.

c. *The advection term*

In RCE simulations with rotation, Wing et al. (2016) showed that the GMSE variance is mainly driven by diabatic heating but damped by the advection. When it comes to TCs simulated in GCMs with realistic boundary conditions, Wing et al. (2019) argued that the advection term is a negative contribution to the development of TCs. However, they pointed out that the advection term computed as a residual may not accurately reflect the impact of advection on TCs. Recently, Wing (2022) further computed the advection term online and showed its negative contribution to the development of TCs in a set of idealized simulations.

Here, we compute the advection term offline using the instantaneous 6-hourly outputs. Instead of directly diving into the advection term, we start with anomalies of the horizontal and vertical convergence of the wind field: $-[(\partial u/\partial x) + (\partial v/\partial y)]'$ and $-[\partial\omega/\partial p]'$. The partial derivatives are computed using centered finite differences. The vertical structure of $-[(\partial u/\partial x) + (\partial v/\partial y)]'$ reflects primary features of TCs, with positive anomalies representing strong radial inflow in the boundary layer while negative ones represent strong radial outflow in the upper troposphere (Fig. 9; the first row). In contrast, $-[\partial\omega/\partial p]'$ exhibits opposite structures (Fig. 9; the first row). Although these terms are computed by the centered finite-difference method using 6-hourly model outputs and subgrid processes are not included, residuals are small (the third row in Fig. 9). However, this method has boundary value problems, which lead to a different number of missing values in the horizontal and vertical dimensions (as shown by the gray shading in Fig. 9).

Brought to you by NOAA Central Library | Unauthenticated | Downloaded 01/30/24 02:51 PM UTC

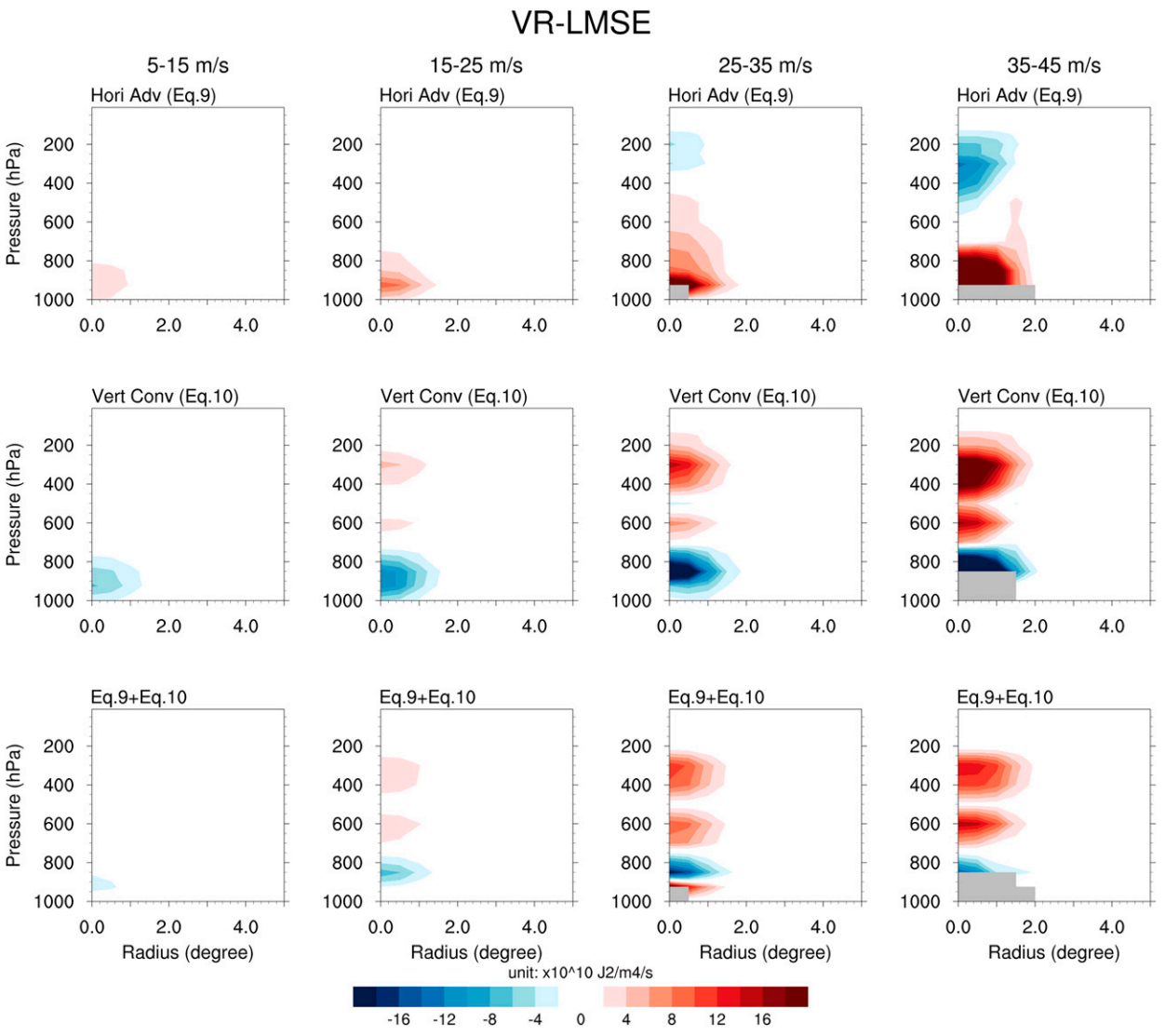

FIG. 11. As in Fig. 1, but for (top) $-\mathrm{LMSE}_i' \times \{[\partial(u_i \times \mathrm{LMSE}_i)/\partial x] + [\partial(v_i \times \mathrm{LMSE}_i)/\partial y]\}'$, (middle) $-\mathrm{LMSE}_i' \times [\partial(\omega_i \times \mathrm{LMSE}_i)/\partial p]'$, and (bottom) the sum of them (units are 1×10^{10} J^2 m^{-4} s^{-1}).

In the VR-LMSE variance framework, both the horizontal and vertical convergence of LMSE flux anomalies can be quantified at individual pressure levels. To have the same physical meaning as the radiation in which positive values mean anomalous heating of the atmosphere to the domain average, we retain the negative sign in front of them and use the two equations listed below:

$$-\left[\frac{\partial(u_i \times \mathrm{LMSE}_i)}{\partial x} + \frac{\partial(v_i \times \mathrm{LMSE}_i)}{\partial y}\right]', \tag{7}$$

$$-\left[\frac{\partial(\omega_i \times \mathrm{LMSE}_i)}{\partial p}\right]'. \tag{8}$$

For the horizontal component [Eq. (7)], positive values are found in the boundary layer, which indicates strong convergence of MSE into the center of TCs. Such positive values intensify as TCs get stronger. In the upper troposphere, negative values indicate horizontal divergence of MSE (Fig. 10, the top row). The vertical component [Eq. (8)] exhibits opposite vertical structure in general: positive anomalies are mainly found in the mid–upper troposphere, while negative anomalies appear in the boundary layer (Fig. 10, the middle row). The positive anomalies reflect upward transport of MSE by convection. More importantly, we note that the MSE convergence shown in Fig. 10 has the same units (W m^{-2}) as LW and SW radiation shown in Fig. 1, but the order of magnitude is much larger than that of radiation, indicating greater local contribution by the MSE convergence than radiation.

We further our analyses by computing the horizontal and vertical components of the advection term, which are

Brought to you by NOAA Central Library | Unauthenticated | Downloaded 01/30/24 02:51 PM UTC

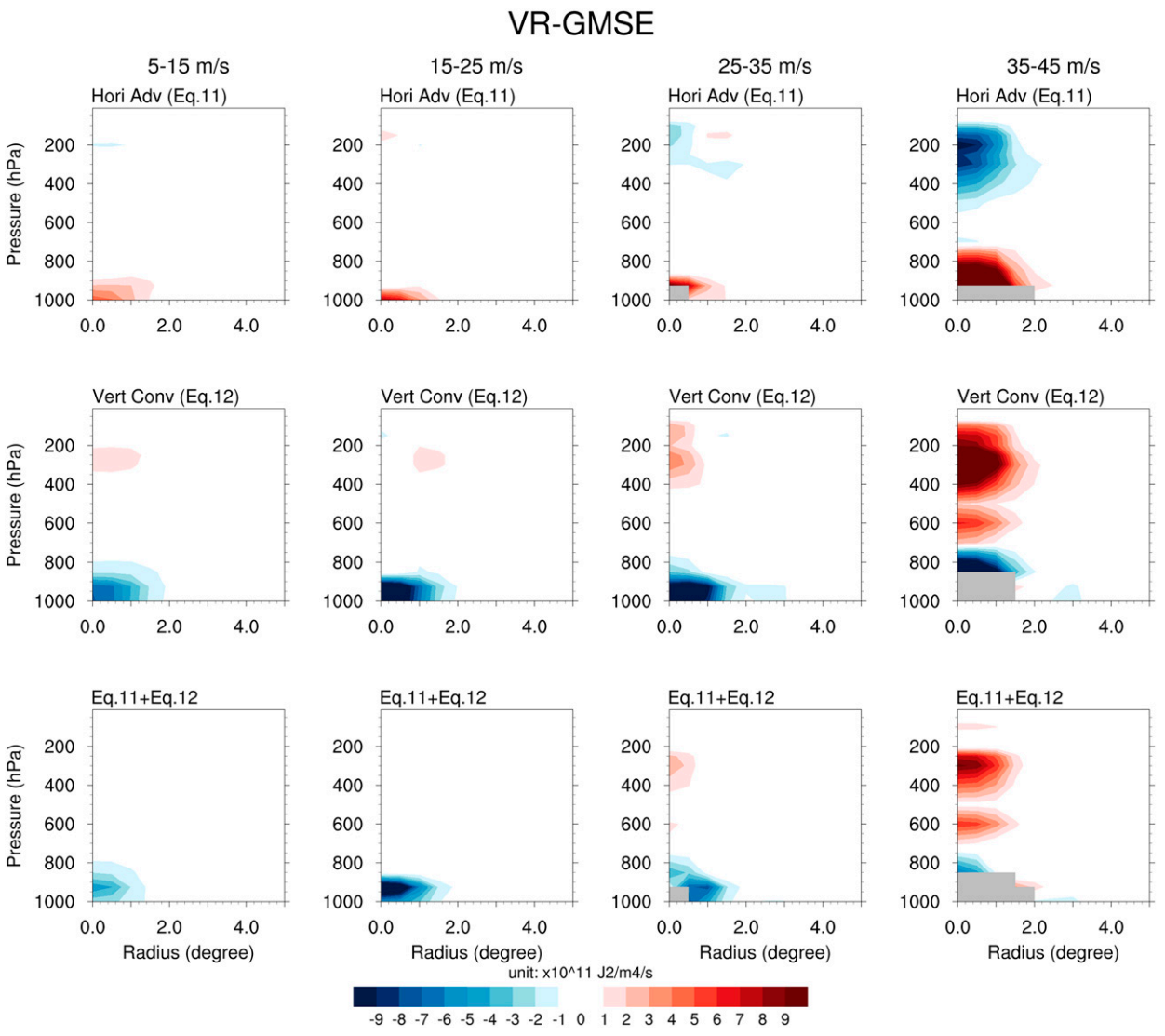

FIG. 12. As in Fig. 1, but for (top) $-\mathrm{GMSE}' \times \{[\partial(u_i \times \mathrm{LMSE}_i)/\partial x] + [\partial(v_i \times \mathrm{LMSE}_i)/\partial y]\}'$, (middle) $\mathrm{GMSE}' \times [\partial(\omega_i \times \mathrm{LMSE}_i)/\partial p]'$, and (bottom) the sum of them (units are $1 \times 10^{11}\ \mathrm{J^2\ m^{-4}\ s^{-1}}$).

$$-\mathrm{LMSE}_i' \times \left[\frac{\partial(u_i \times \mathrm{LMSE}_i)}{\partial x} + \frac{\partial(v_i \times \mathrm{LMSE}_i)}{\partial y}\right]', \tag{9}$$

$$-\mathrm{LMSE}_i' \times \left[\frac{\partial(\omega_i \times \mathrm{LMSE}_i)}{\partial p}\right]'. \tag{10}$$

Physically, these two terms represent interactions between anomalous LMSE and the convergence of LMSE in the horizontal and vertical directions, respectively. If positive anomalies of the convergence are coincident with positive anomalies of LMSE_i', the advection term will further increase the already positive anomalies of LMSE_i', which is regarded as positive feedback. With this in mind, Fig. 11 shows the terms defined in Eqs. (9) and (10). Overall, these two terms show similar vertical structures as in Fig. 10: both terms increase as TCs get stronger, with positive anomalies of the horizontal component found mostly in the boundary layer (Fig. 11, the first row), whereas positive anomalies of the vertical component are mainly found in the mid–upper troposphere (Fig. 11, the second row). The total contribution by the advection in the VR-LMSE framework can be positive, especially in the mid–upper troposphere that is dominated by the vertical component (Fig. 11, the third row).

In addition, we compute the horizontal and vertical components of the advection term in the VR-GMSE framework using

$$-\mathrm{GMSE}' \times \left[\frac{\partial(u_i \times \mathrm{LMSE}_i)}{\partial x} + \frac{\partial(v_i \times \mathrm{LMSE}_i)}{\partial y}\right]', \tag{11}$$

$$-\mathrm{GMSE}' \times \left[\frac{\partial(\omega_i \times \mathrm{LMSE}_i)}{\partial p}\right]'. \tag{12}$$

Brought to you by NOAA Central Library | Unauthenticated | Downloaded 01/30/24 02:51 PM UTC

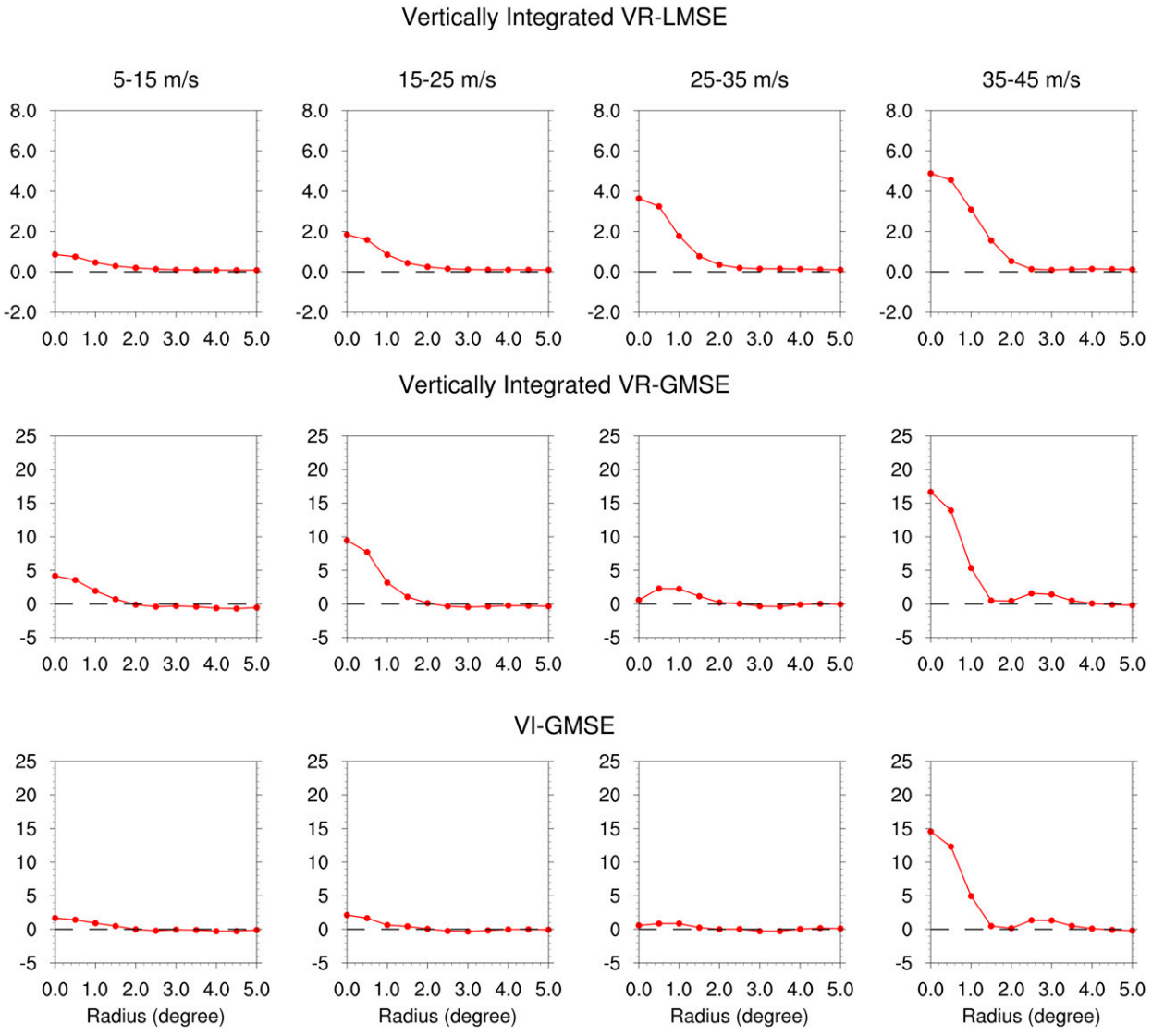

FIG. 13. Vertical integrated values of the horizontal component of the advection term (units are 1×10^{11} J^2 m^{-4} s^{-1}) computed in the (top) VR-LMSE, (middle) VR-GMSE, and (bottom) VI-GMSE frameworks during different TC intensities: 5–15, 15–25, 25–35, and 35–45 m s^{-1}. Note that ranges of y axis are different between these frameworks.

Vertical structures of the advection term in the VR-GMSE framework (Fig. 12) are similar to those in the VR-LMSE framework (Fig. 11), except that the order of magnitude is larger in the VR-GMSE framework.

In the VR-LMSE and VR-GMSE frameworks, the horizontal and vertical components of the advection term exhibit vertically varied contributions to the development of TCs. A vertically integrated analysis of the horizontal component shows positive values (Fig. 13). Note that the first two rows in Fig. 13 correspond to the first row in Fig. 11 and the first row in Fig. 12, respectively. However, since the horizontal component is tightly connected with the vertical component due to the continuity equation, this only reflects significant radial inflow in the boundary layer associated with TCs.

4. Summary and discussion

In this study, we examine the vertical structure of interactions between radiation, circulation, and MSE associated with TCs simulated in a GCM under realistic boundary conditions. The sign of radiative interactions associated with TCs changes vertically. Although perturbations in SW radiation are negative, those in LW radiation are positive and stronger in magnitude, leading to overall positive radiative feedback that promotes the development of TCs. We compare the role of radiative interactions in the boundary layer with those in the free troposphere in the development of TCs by doing mechanism-denial experiments. Qualitatively, the global TC frequency is reduced in both cases. Suppressing synoptic-scale radiative interactions in the boundary layer yields comparable magnitude of reduction in

Brought to you by NOAA Central Library | Unauthenticated | Downloaded 01/30/24 02:51 PM UTC

global TC frequency as suppressing radiative interactions in the free troposphere, even though the boundary layer accounts for a smaller part of the atmosphere than the free troposphere. However, stronger TCs (category 1–5 TCs) exhibit more reduction when radiative interactions are suppressed in the free troposphere than in the boundary layer. In general, stronger TCs have deeper and higher clouds than weaker ones, which results in significant radiative perturbations in the mid- to upper levels. Such radiative perturbations are missing in the ClimRadFT run, which could explain the greater reduction in stronger TCs.

To understand the reduction in global TC frequency, we compare various frameworks that focus on either LMSE variance or GMSE variance following a recent paper on convective aggregation by Yao et al. (2021). Although there is no consensus in terms of which framework is the best, the vertical distribution of the feedbacks is shown to be crucial in understanding the changes in global TC frequency. However, the covariance terms raise further issues that warrant future study. Given that the covariance terms can potentially change the sign of the vertical integral, a sound physical explanation of their contribution is required (Yao et al. 2021). Otherwise, it could be problematic to interpret the vertical integral simply based on the sign.

In addition, we explicitly computed the advection term using instantaneous 6-hourly outputs. In general, the order of magnitude of MSE convergence is much larger than that of radiation, indicating greater local contribution by MSE convergence than radiation. Near the TC center, the horizontal component of the advection term is mainly positive in the boundary layer, while the vertical component is positive from the mid- to upper levels of the troposphere, reflecting the upward transport of MSE by convection. However, these positive values do not necessarily imply further TC development. It is worth mentioning that the analyses in this study focus on domains following the movement of the tracked TCs. Therefore, background conditions (e.g., the large-scale circulation) can be different across the domains of the tracked TCs.

Nonetheless, the VR analyses including the advection term provide more process-oriented information of physical processes associated with TCs under realistic boundary conditions. Future work can apply the VR framework to a broader range of conditions such as experiments with background winds versus those without background winds. The VR analyses help us understand physical processes associated with TCs at different levels, which is key to model simulations and future projections of TCs.

Acknowledgments. This research was supported by NOAA Awards NA18OAR4310269 and NA18OAR4310418 and Department of Energy Award DE-SC0021333. We thank three anonymous reviewers for their helpful suggestions and comments.

Data availability statement. HiRAM simulations are performed on the Princeton University Research Computing systems. The datasets produced in this study are available upon request.

REFERENCES

Bretherton, C. S., P. N. Blossey, and M. Khairoutdinov, 2005: An energy-balance analysis of deep convective self-aggregation above uniform SST. *J. Atmos. Sci.*, **62**, 4273–4292, https://doi.org/10.1175/JAS3614.1.

Broccoli, A. J., and S. Manabe, 1990: Can existing climate models be used to study anthropogenic changes in tropical cyclone climate? *Geophys. Res. Lett.*, **17**, 1917–1920, https://doi.org/10.1029/GL017i011p01917.

Camargo, S. J., 2013: Global and regional aspects of tropical cyclone activity in the CMIP5 models. *J. Climate*, **26**, 9880–9902, https://doi.org/10.1175/JCLI-D-12-00549.1.

——, and Coauthors, 2020: Characteristics of model tropical cyclone climatology and the large-scale environment. *J. Climate*, **33**, 4463–4487, https://doi.org/10.1175/JCLI-D-19-0500.1.

Duvel, J.-P., S. J. Camargo, and A. H. Sobel, 2017: Role of the convection scheme in modeling initiation and intensification of tropical depressions over the North Atlantic. *Mon. Wea. Rev.*, **145**, 1495–1509, https://doi.org/10.1175/MWR-D-16-0201.1.

Feng, J., and Y. Huang, 2021: Impacts of tropical cyclones on the thermodynamic conditions in the tropical tropopause layer observed by A-Train satellites. *Atmos. Chem. Phys.*, **21**, 15 493–15 518, https://doi.org/10.5194/acp-21-15493-2021.

Gray, W. M., and R. W. Jacobson Jr., 1977: Diurnal variation of deep cumulus convection. *Mon. Wea. Rev.*, **105**, 1171–1188, https://doi.org/10.1175/1520-0493(1977)105<1171:DVODCC>2.0.CO;2.

Harris, L. M., S.-J. Lin, and C. Tu, 2016: High-resolution climate simulations using GFDL HiRAM with a stretched global grid. *J. Climate*, **29**, 4293–4314, https://doi.org/10.1175/JCLI-D-15-0389.1.

Jeevanjee, N., and D. M. Romps, 2013: Convective self-aggregation, cold pools, and domain size. *Geophys. Res. Lett.*, **40**, 994–998, https://doi.org/10.1002/grl.50204.

Manabe, S., J. L. Holloway Jr., and H. M. Stone, 1970: Tropical circulation in a time-integration of a global model of the atmosphere. *J. Atmos. Sci.*, **27**, 580–613, https://doi.org/10.1175/1520-0469(1970)027<0580:TCIATI>2.0.CO;2.

Mapes, B. E., 2016: Gregarious convection and radiative feedbacks in idealized worlds. *J. Adv. Model. Earth Syst.*, **8**, 1029–1033, https://doi.org/10.1002/2016MS000651.

Melhauser, C., and F. Zhang, 2014: Diurnal radiation cycle impact on the pregenesis environment of Hurricane Karl (2010). *J. Atmos. Sci.*, **71**, 1241–1259, https://doi.org/10.1175/JAS-D-13-0116.1.

Muller, C. J., and I. M. Held, 2012: Detailed investigation of the self-aggregation of convection in cloud-resolving simulations. *J. Atmos. Sci.*, **69**, 2551–2565, https://doi.org/10.1175/JAS-D-11-0257.1.

——, and S. Bony, 2015: What favors convective aggregation and why? *Geophys. Res. Lett.*, **42**, 5626–5634, https://doi.org/10.1002/2015GL064260.

——, and D. M. Romps, 2018: Acceleration of tropical cyclogenesis by self-aggregation feedbacks. *Proc. Natl. Acad. Sci. USA*, **115**, 2930–2935, https://doi.org/10.1073/pnas.1719967115.

Murakami, H., and Coauthors, 2012: Future changes in tropical cyclone activity projected by the new high-resolution MRI-AGCM. *J. Climate*, **25**, 3237–3260, https://doi.org/10.1175/JCLI-D-11-00415.1.

——, and Coauthors, 2015: Simulation and prediction of category 4 and 5 hurricanes in the high-resolution GFDL HiFLOR

Brought to you by NOAA Central Library | Unauthenticated | Downloaded 01/30/24 02:51 PM UTC

coupled climate model. *J. Climate*, **28**, 9058–9079, https://doi.org/10.1175/JCLI-D-15-0216.1.

——, E. Levin, T. L. Delworth, R. Gudgel, and P.-C. Hsu, 2018: Dominant effect of relative tropical Atlantic warming on major hurricane occurrence. *Science*, **362**, 794–799, https://doi.org/10.1126/science.aat6711.

Neelin, J. D., and I. M. Held, 1987: Modeling tropical convergence based on the moist static energy budget. *Mon. Wea. Rev.*, **115**, 3–12, https://doi.org/10.1175/1520-0493(1987)115<0003:MTCBOT>2.0.CO;2.

Nicholls, M. E., 2015: An investigation of how radiation may cause accelerated rates of tropical cyclogenesis and diurnal cycles of convective activity. *Atmos. Chem. Phys.*, **15**, 9003–9029, https://doi.org/10.5194/acp-15-9003-2015.

Rayner, N. A., D. E. Parker, E. B. Horton, C. K. Folland, L. V. Alexander, D. P. Rowell, E. C. Kent, and A. Kaplan, 2003: Global analyses of sea surface temperature, sea ice, and night marine air temperature since the late nineteenth century. *J. Geophys. Res.*, **108**, 4407, https://doi.org/10.1029/2002JD002670.

Rios-Berrios, R., 2020: Impacts of radiation and cold pools on the intensity and vortex tilt of weak tropical cyclones interacting with vertical wind shear. *J. Atmos. Sci.*, **77**, 669–689, https://doi.org/10.1175/JAS-D-19-0159.1.

Roberts, M. J., and Coauthors, 2015: Tropical cyclones in the UPSCALE ensemble of high-resolution global climate models. *J. Climate*, **28**, 574–596, https://doi.org/10.1175/JCLI-D-14-00131.1.

Ruppert, J. H., Jr., A. A. Wing, X. Tang, and E. L. Duran, 2020: The critical role of cloud–infrared radiation feedback in tropical cyclone development. *Proc. Natl. Acad. Sci. USA*, **117**, 27 884–27 892, https://doi.org/10.1073/pnas.2013584117.

Shaevitz, D. A., and Coauthors, 2014: Characteristics of tropical cyclones in high-resolution models in the present climate. *J. Adv. Model. Earth Syst.*, **6**, 1154–1172, https://doi.org/10.1002/2014MS000372.

Smith, W. P., M. E. Nicholls, and R. A. Pielke Sr., 2020: The role of radiation in accelerating tropical cyclogenesis in idealized simulations. *J. Atmos. Sci.*, **77**, 1261–1277, https://doi.org/10.1175/JAS-D-19-0044.1.

Tang, X., and F. Zhang, 2016: Impacts of the diurnal radiation cycle on the formation, intensity, and structure of Hurricane Edouard (2014). *J. Atmos. Sci.*, **73**, 2871–2892, https://doi.org/10.1175/JAS-D-15-0283.1.

——, Z.-M. Tan, J. Fang, Y. Q. Sun, and F. Zhang, 2017: Impact of the diurnal radiation cycle on secondary eyewall formation. *J. Atmos. Sci.*, **74**, 3079–3098, https://doi.org/10.1175/JAS-D-17-0020.1.

——, ——, ——, E. B. Munsell, and F. Zhang, 2019: Impact of the diurnal radiation contrast on the contraction of radius of maximum wind during intensification of Hurricane Edouard (2014). *J. Atmos. Sci.*, **76**, 421–432, https://doi.org/10.1175/JAS-D-18-0131.1.

Trabing, B. C., M. M. Bell, and B. R. Brown, 2019: Impacts of radiation and upper-tropospheric temperatures on tropical cyclone structure and intensity. *J. Atmos. Sci.*, **76**, 135–153, https://doi.org/10.1175/JAS-D-18-0165.1.

Vecchi, G. A., and Coauthors, 2014: On the seasonal forecasting of regional tropical cyclone activity. *J. Climate*, **27**, 7994–8016, https://doi.org/10.1175/JCLI-D-14-00158.1.

——, and Coauthors, 2019: Tropical cyclone sensitivities to CO_2 doubling: Roles of atmospheric resolution, synoptic variability and background climate changes. *Climate Dyn.*, **53**, 5999–6033, https://doi.org/10.1007/s00382-019-04913-y.

Walsh, K. J. E., M. Fiorino, C. Landsea, and K. L. McInnes, 2007: Objectively determined resolution-dependent threshold criteria for the detection of tropical cyclones in climate models and reanalyses. *J. Climate*, **20**, 2307–2314, https://doi.org/10.1175/JCLI4074.1.

——, and Coauthors, 2015: Hurricanes and climate: The U.S. CLIVAR working group on hurricanes. *Bull. Amer. Meteor. Soc.*, **96**, 997–1017, https://doi.org/10.1175/BAMS-D-13-00242.1.

Wehner, M., Prabhat, K. A. Reed, D. Stone, W. D. Collins, and J. Bacmeister, 2015: Resolution dependence of future tropical cyclone projections of CAM5.1 in the U.S. CLIVAR hurricane working group idealized configurations. *J. Climate*, **28**, 3905–3925, https://doi.org/10.1175/JCLI-D-14-00311.1.

Wing, A. A., 2022: Acceleration of tropical cyclone development by cloud-radiative feedbacks. *J. Atmos. Sci.*, **79**, 2285–2305, https://doi.org/10.1175/JAS-D-21-0227.1.

——, and K. A. Emanuel, 2014: Physical mechanisms controlling self-aggregation of convection in idealized numerical modeling simulations. *J. Adv. Model. Earth Syst.*, **6**, 59–74, https://doi.org/10.1002/2013MS000269.

——, S. J. Camargo, and A. H. Sobel, 2016: Role of radiative–convective feedbacks in spontaneous tropical cyclogenesis in idealized numerical simulations. *J. Atmos. Sci.*, **73**, 2633–2642, https://doi.org/10.1175/JAS-D-15-0380.1.

——, and Coauthors, 2019: Moist static energy budget analysis of tropical cyclone intensification in high-resolution climate models. *J. Climate*, **32**, 6071–6095, https://doi.org/10.1175/JCLI-D-18-0599.1.

Wu, S.-N., B. J. Soden, and D. S. Nolan, 2021: Examining the role of cloud radiative interactions in tropical cyclone development using satellite measurements and WRF simulations. *Geophys. Res. Lett.*, **48**, e2021GL093259, https://doi.org/10.1029/2021GL093259.

Yang, D., 2018a: Boundary layer diabatic processes, the virtual effect, and convective self-aggregation. *J. Adv. Model. Earth Syst.*, **10**, 2163–2176, https://doi.org/10.1029/2017MS001261.

——, 2018b: Boundary layer height and buoyancy determine the horizontal scale of convective self-aggregation. *J. Atmos. Sci.*, **75**, 469–478, https://doi.org/10.1175/JAS-D-17-0150.1.

Yao, L., and D. Yang, 2021: Vertically-resolved moist static energy diagnosis on the development of tropical cyclones. *2021 Fall Meeting*, New Orleans, LA, Amer. Geophys. Union, Abstract A25D-1713.

——, ——, and Z.-M. Tan, 2021: A vertically resolved MSE framework highlights the role of the boundary layer in convective self-aggregation. *J. Atmos. Sci.*, **79**, 1615–1631, https://doi.org/10.1175/JAS-D-20-0254.1.

Zhang, B., B. J. Soden, G. A. Vecchi, and W. Yang, 2021a: The role of radiative interactions in tropical cyclone development under realistic boundary conditions. *J. Climate*, **34**, 2079–2091, https://doi.org/10.1175/JCLI-D-20-0574.1.

——, ——, ——, and ——, 2021b: Investigating the causes and impacts of convective aggregation in a high resolution atmospheric GCM. *J. Adv. Model. Earth Syst.*, **13**, e2021MS002675, https://doi.org/10.1029/2021MS002675.

Zhao, M., I. M. Held, S.-J. Lin, and G. A. Vecchi, 2009: Simulations of global hurricane climatology, interannual variability, and response to global warming using a 50-km resolution GCM. *J. Climate*, **22**, 6653–6678, https://doi.org/10.1175/2009JCLI3049.1.

——, ——, and ——, 2012: Some counterintuitive dependencies of tropical cyclone frequency on parameters in a GCM. *J. Atmos. Sci.*, **69**, 2272–2283, https://doi.org/10.1175/JAS-D-11-0238.1.

Brought to you by NOAA Central Library | Unauthenticated | Downloaded 01/30/24 02:51 PM UTC